Available online at www.sciencedirect.com
SCIENCE DIRECT®
Nuclear Instruments and Methods in Physics Research A 550 (2005) 397–413
NUCLEAR INSTRUMENTS & METHODS IN PHYSICS RESEARCH Section A
www.elsevier.com/locate/nima

Characteristics of a lead slowing-down spectrometer coupled to the LANSCE accelerator

D. Rochman[a,1], R.C. Haight[a,*], J.M. O' Donnell[a], A. Michaudon[a], S.A. Wender[a], D.J. Vieira[b], E.M. Bond[b], T.A. Bredeweg[b], A. Kronenberg[b,2], J.B. Wilhelmy[b], T. Ethvignot[c], T. Granier[c], M. Petit[c], Y. Danon[d]

[a]*LANSCE-3, Los Alamos National Laboratory, MS H855, Los Alamos, NM 87545, USA*
[b]*C-INC, Los Alamos National Laboratory, MS J514, Los Alamos, NM 87545, USA*
[c]*Commissariat à l'Énergie Atomique, DIF/DPTA/Service de Physique Nucléaire, BP 12, 91680 Bruyères-le-Châtel, France*
[d]*Rensselaer Polytechnic Institute, Troy, New York, NY 12180, USA*

Received 28 January 2005; received in revised form 19 April 2005; accepted 25 April 2005
Available online 20 July 2005

Abstract

A description is given of a lead slowing-down spectrometer (LSDS) installed at the 800-MeV proton accelerator of the Los Alamos Neutron Science Center (LANSCE). The LSDS is designed to study neutron-induced fission on actinides that can only be obtained or used in small quantities. The characteristics of this LSDS (energy–time relation, energy resolution, neutron flux) are presented through simulations with MCNPX and measurements with several different methods. Results on neutron-induced fission of ^{235}U and ^{239}Pu with tens of micrograms and tens of nanograms, respectively, are presented. Finally, additional MCNPX calculations have been performed to simulate the measurement of the cross-section for ^{235m}U(n, f) using different target quantities and different initial isomer-to-ground state compositions.

PACS: 25.85.Ec; 29.25.Dz; 29.27.Fh; 29.30.Hs

Keywords: Neutron-induced reaction; Lead slowing-down spectrometer; Spallation neutron source; Fission cross-section; MCNPX

*Corresponding author. Tel.: +1 505 667 2829; fax: +1 505 665 3705.
E-mail addresses: drochman@bnl.gov (D. Rochman), haight@lanl.gov (R.C. Haight), odonnell@lanl.gov (J.M. O' Donnell), michaudon@lanl.gov (A. Michaudon), wender@lanl.gov (S.A. Wender), vieira@lanl.gov (D.J. Vieira), bond@lanl.gov (E.M. Bond), toddb@lanl.gov (T.A. Bredeweg), kronenberga@mail.phy.ornl.gov (A. Kronenberg), j_wilhelmy@lanl.gov (J.B. Wilhelmy), thierry.ethvignot@cea.fr (T. Ethvignot), thierry.granier@cea.fr (T. Granier), michael.petit@cea.fr (M. Petit), danony@rpi.edu (Y. Danon).
[1]Present address: National Nuclear Data Center, Brookhaven National Laboratory, Upton, NY 11973, USA.
[2]Present address: Oak Ridge Associated Universities, Oak Ridge, TN 37831, USA.

0168-9002/$ - see front matter © 2005 Elsevier B.V. All rights reserved.
doi:10.1016/j.nima.2005.04.075

1. Introduction

Knowledge of cross-sections for neutron-induced fission of actinides is important for understanding processes that occur in reactors, accelerator-driven systems and nuclear explosions. In a very high neutron flux environment, the yield from fission reactions depends not only on the fission cross-sections of nuclei in their ground states, but also on the fission cross-sections of nuclei in isomeric states, which can be populated by neutron inelastic scattering, neutron capture or radioactive decay. The neutron economy can be significantly modified if a difference exists between the isomer and the ground state fission cross-sections. Because of their short half-lives, low production yields in the laboratory, or handling limitations, some of these isomers can only be obtained and used in small quantities for experiments. As a consequence, the count rates in conventional beam-target experiments are low. The same constraint may exist for fission cross-section measurements on other samples that can be obtained or handled only in small quantities.

To compensate for the low count rates resulting from small samples, a very high neutron flux is needed to make a measurement. With the goal of performing such measurements, we have developed a lead slowing-down spectrometer (LSDS) at LANSCE following the suggestion of Moore et al. [1]. Herein we summarize the initial performance results of the LSDS for the neutron-induced fission cross-section measurements using small quantities of actinides. This work will also test and validate the simulations performed previously in Ref. [2].

An LSDS dedicated to the measurements of neutron-induced reaction cross-sections as a function of incident neutron energy can yield neutron fluxes up to 10^4 times higher than those in conventional time-of-flight [TOF] experiments [3]. The spectrometer consists of a large block of high-purity lead (typically greater than 1 m^3 in volume), inside of which pulses of fast neutrons are produced by bombarding a neutron-producing target with a charged-particle beam (electrons, protons or deuterons) [4]. The neutrons are essentially trapped in the lead for hundreds of microseconds due to the very small capture cross-section, and they lose only a small quantity of energy at each elastic collision with a Pb nucleus. The scattering cross-section is very nearly constant and that results in a correlation ($E_n \propto 1/(t+t_0)^2$) between the slowing-down time and the neutron energy inside the lead cube [5]. Because the neutrons are trapped, the neutron flux incident on a sample inside the lead is greatly increased and thus the count rates for a sample and detector inside the lead are much higher than in the open geometry of a conventional TOF facility; but in return, the neutron energy resolution is limited, unlike conventional time-of-flight experiments where in principle, the resolution can always be improved by going to a longer flight path. A simulation carried out with the Monte Carlo radiation transport code MCNPX 2.5d [6] of the neutron flux as a function of time after the proton pulse is presented qualitatively in Fig. 1. This figure illustrates that for a given time, the spread in neutron energy is important. For example, the energy resolution $\Delta E/\bar{E}$ is at best on the order of 30% (FWHM) [3].

Since the first LSDS built in 1955 [5], a number of similar devices have been constructed worldwide

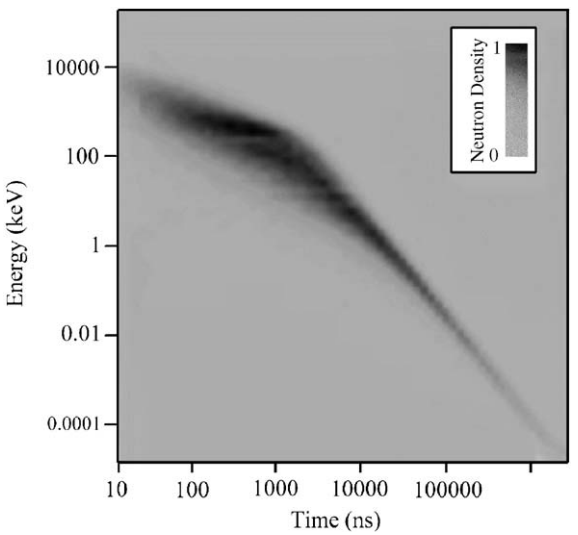

Fig. 1. Simulation of the relative neutron density as a function of time ($t = 0$ is the origin of the spallation process) at a typical location in the LSDS. Note that for times greater than 1 μs, there is a "focusing" of the neutrons to an approximate time–energy relationship.

[2,4,7–14]. These instruments are driven by pulsed fast neutrons generated at or near the center of the lead assembly. The neutrons then undergo numerous elastic and inelastic scatterings in the process of slowing down. When their energies become less than that necessary for inelastic scattering, about 0.5 MeV, all of the interactions are elastic, except for a very small fraction that is lost due to neutron capture. Because the energy loss in an elastic collision is small on average, the neutrons lose energy slowly and a correspondence develops between the time and the mean neutron energy as shown in Fig. 1. Several types of measurements have been performed with an LSDS:

- fission cross-sections of actinides that are available or usable in only small quantities: ^{244,246,248}Cm [15,16], ^{242}Cm and ^{238}Pu [17], ^{254}Es and ^{250}Cf [18], ^{229}Th and ^{231}Pa [19], ^{232}Pa and $^{236,\ 238}$Np [20],
- measurement of small, sub-threshold fission cross-sections: ^{232}Th [21,22], ^{238}U [23,24],
- resonance capture γ-ray spectroscopy [12]
- long-lived transmutation of fission fragments [13],
- capture cross-sections of ^{232}Th, ^{nat}U, and ^{99}Tc [25], ^{237}Np [26].

An interesting example of a short-lived isomer is the first excited state of uranium 235 with an half-life of 26 min [27]. The transition energy has been determined to be at 76.8 ± 0.5 eV [28]. Until now, the ratio of the isomer fission cross-section to the ground state fission cross-section (σ_m/σ_g) has been measured only for thermal and cold neutron energies [29–31]. For these low energies, the fission cross-section for the isomer is larger than that for the ground state by a factor in the range of 1.42 to 2.47, where the range reflects some disagreements in the reported experimental results. At higher energies, recent theoretical calculations predict instead that the fission cross-section of the isomer is less than that for the ground state at 1 keV by a factor of 0.7. The two cross-sections become approximately equal at 500 keV [33,34]. In the laboratory, this isomer can be produced from the α-decay of ^{239}Pu, but because of its relatively short half-life, only nanogram quantities of the isomer exist in secular equilibrium with grams of ^{239}Pu (the equilibrium ratio being $2 \cdot 10^{-9}$). It is therefore a candidate for measurements with the LSDS. Following the results of simulations given in Ref. [2], it should be possible to measure the neutron-induced fission cross-section with good statistical accuracy from 1 eV to 100 keV.

2. Experiment

2.1. Lead cube

The basic features of the LSDS are listed below. It consists of 36 blocks, each made from high-purity lead, $40 \times 40 \times 30\,\text{cm}^3$ and 542 kg in mass. These blocks are assembled to form a cube, 1.2 m on a side with a total mass of 19.5 tons. This spectrometer was previously used at the CEA laboratory at Bruyères-le-Châtel, France, for isomer production [35]. In each block a channel allows samples and detectors to be inserted for measurements. At the center of the LSDS, two channels facing each other serve as the entrance channel for the proton beam. Each channel has a width of 10.1 cm and a height of 5.1 cm, see Fig. 2(left).

2.2. Neutron source

At the center of the lead volume, neutrons are produced by the spallation process between the proton beam and a stopping-length tungsten target. In Fig. 2(right), the result of the MCNPX calculation presents the neutron production and their trajectories within the LSDS and up to 100 cm from its center from the interaction between a single 800-MeV proton and the tungsten target. As mentioned previously, most of the neutrons stay inside the lead volume for hundreds of microseconds and a significant number remain for several milliseconds.

This LSDS is now located at the Los Alamos Neutron Science Center (LANSCE). The linear accelerator provides a beam of 800-MeV protons; the proton intensity, available at the spectrometer is at present limited by radiation safety considerations to 1 μA average current. To obtain short

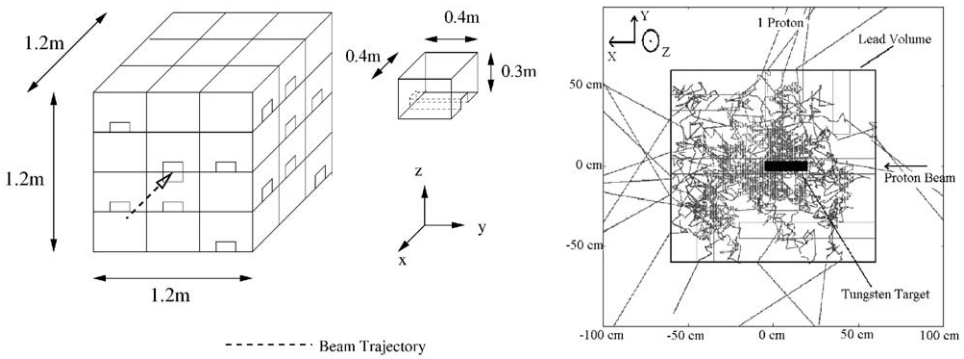

Fig. 2. Left: Layout of the lead slowing-down spectrometer, with channels in each block. Right: MCNPX simulation of the neutron production and their flight paths from the interaction between one proton and the tungsten target.

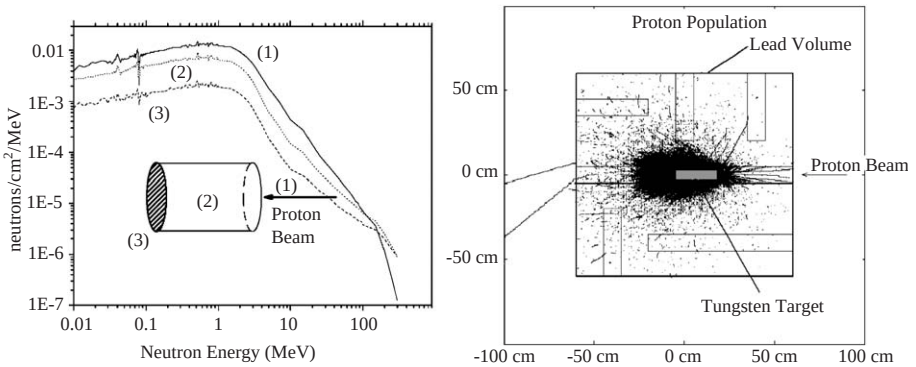

Fig. 3. Left: Neutron flux as a function of neutron energy at the three faces of the tungsten target. Right: Proton population in the LSDS as a function of X and Y through a layer 2 cm thick centered at $Z = 0$. The 800-MeV proton beam is coming from the right, through an empty channel and interacts with the tungsten target at the center of the lead volume.

proton pulses, a 30-m diameter proton storage ring (PSR) compresses the 750-μs proton pulses from the linac into pulses of typically 250–300 ns. The highest frequency delivered at present by the PSR is 20 Hz. At low proton beam intensity, e.g. 300 nA average current, the beam pulses can be significantly shorter, for example, with burst widths shorter than 20 ns at a repetition rate of 20 Hz.

The proton beam is transported to the LSDS at the center of the Blue Room (Target 2) of the Weapons Neutron Research facility [36]. This room has a specially designed low-mass floor made of aluminum and a 4.4 m deep basement which limits the number of room-backscattered neutrons reaching the lead spectrometer. The diameter of the room is $\simeq 12.2$ m and the parabolic roof is 7 m above the floor. At the tungsten target position, the proton beam has approximately a Gaussian distribution with $\sigma = 0.46$ cm [37].

Secondary neutron production is realized through spallation in a stopping-length tungsten target. The tungsten target is a cylinder 25 cm long and 7 cm in diameter, which was chosen to contain most of the multiple-scattered proton beam. Tungsten was chosen because of its large atomic mass and density (18.4 g cm^{-3} as received), providing a high neutron production in a small volume. In the case of a tungsten cylinder 25 cm long, the number of neutrons emitted per 800 MeV proton is between 13 and 14 and the neutron flux, calculated with MCNPX, is presented in Fig. 3(left).

This spectrum from the tungsten is a typical spallation neutron flux with a maximum at ≈ 2 MeV. More neutrons are produced upstream,

but the energy-dependent flux shape is very similar on all sides of the target. Even if the proton stopping length is shorter than the target length, some protons can exit the tungsten by scattering and then interacting with the surrounding lead. An MCNPX simulation is shown in Fig. 3(right) where the proton population is presented as a function of X and Y axis through a Z layer of 2 cm at the center of the LSDS. Some activation of the lead is inevitable and the proton–lead interaction produces prompt gamma rays, commonly called a "gamma flash", which can disturb the detectors and electronics. Because of these scattered protons, the detectors cannot be too close to the target (>15 cm), but they must also not be too far from the target near the outer edge of the lead where the neutron flux decreases rapidly (<55 cm).

2.3. Influence of the lead impurities and the Blue Room environment

Each block is made of high-purity lead with the natural isotopic composition. The lead isotopes mainly differ by their thresholds and cross-sections for inelastic scattering and by their neutron-capture cross-sections. The purity of the lead is such that the impurities have only a small effect on the neutron flux. In practice, three common impurities are most important because of their large neutron-capture cross-sections: silver, antimony and cadmium. A chemical analysis shows that the concentrations for these impurities are 41 ± 6 ppm, 1.4 ± 0.2 ppm and less than 0.029 ppm, respectively. The component blocks of the lead assembly are much larger than traditional $20 \times 10 \times 5\,\text{cm}^3$ bricks so that the surface area of the blocks is small and therefore the effect of hydrogen and oxygen from any water contaminant on the surfaces is reduced.

The geometry of the Blue Room limits the number of neutrons that exit the lead volume and then backscatter after interacting with the walls and floor. To further decrease the backscatter of neutrons into the LSDS, a cadmium cover, 0.9 mm thick, is used as an absorber.

To evaluate the influence of the impurities and of the local environment on the characteristics of the LSDS, simulations with MCNPX were carried out. Two geometries were considered: (1) the lead volume, a tungsten spallation source at its center, without influence from the surrounding environment (no room return), and (2) the same configuration but including backscattered neutrons from the Blue Room and the cadmium cover. To evaluate the influence of the impurities on the neutron flux, the geometry (1) is used with and without impurities in the lead volume.

The influence of the Blue Room is simulated at two different positions in the lead volume: $Y = 20$ cm and $Y = 55$ cm from the spallation source, see Fig. 4 upper panel. The simulations concerning the impurities at 30 cm from the tungsten target are presented in Fig. 4 lower panel.

As expected, the neutron flux can be modified by neutrons coming back from the Blue Room. It also changes the energy–time relation of the spectrometer (see simulation at 55 cm from the tungsten target, Fig. 4 upper panel). This modification becomes weaker when approaching the center of the spectrometer.

Fig. 4 lower panel shows that the neutron flux is modified by the presence of the silver impurity in the lead, especially for neutron energies less than 20 eV. The simulation is carried out for pure lead, without the effect of the Blue Room, with and without silver. The same effect is mentioned in Ref. [2] where a notable effect on the neutron flux was found for a silver concentration of 60 ppm. The effects of antimony and cadmium at the measured impurity levels are significantly smaller.

2.4. Data acquisition system

In order to obtain cross-sections from neutron-induced reactions, time measurements of events relative to the proton beam pulse were performed. From this time interval, the corresponding incident neutron energy can be calculated as explained above. Waveform digitizers (Acqiris DC265 with a maximum sampling rate of 500 MS/s), triggered by the timing signal of the proton pulse, were used to record the time-of-flight signals from a detector, after passing through a discriminator. The waveforms were analyzed in real time to extract the leading edge with a resolution of 50 ns. The time

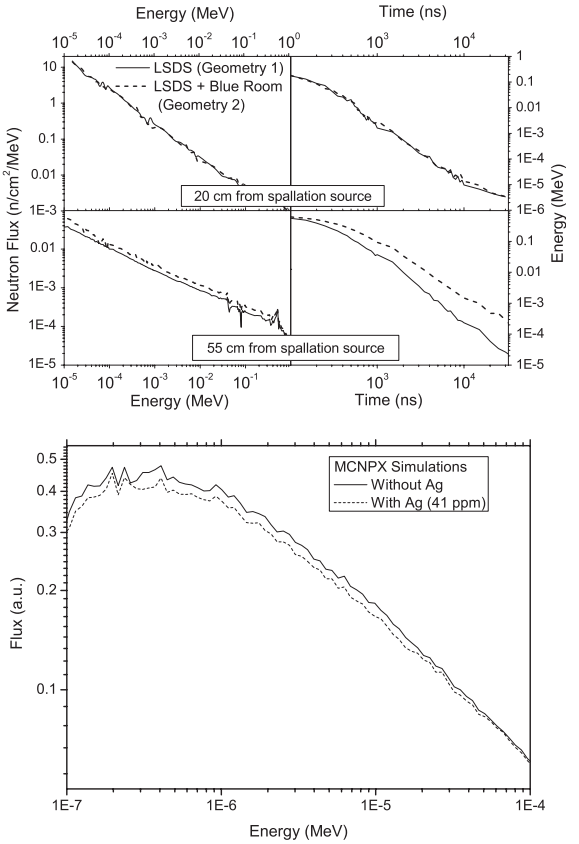

Fig. 4. Upper panel: neutron flux as a function of neutron energy and mean neutron energy as a function of time at $Y = 20$ (upper half) and $Y = 55$ cm (lower half) from the tungsten target averaged over those surfaces. Two geometries are considered: (1) lead and tungsten target and (2) LSDS and the Blue Room. See text for geometry explanations. Lower panel: neutron flux in the LSDS without and with silver (41 ppm).

spectra were recorded to disk using the MIDAS [38] data acquisition system with the ROOT [39] analysis and display package.

3. Lead slowing-down spectrometer characteristics

To characterize the LSDS, measurements of capture and fission were performed on samples with masses of micrograms to milligrams. These reactions provide information on the energy–time relation, energy resolution and neutron flux at different positions. Results are then used to extract cross-sections from measurements on fission with much smaller samples.

3.1. Energy–time correlation

As shown previously in the literature (e.g. Ref. [5]), the neutron energy–time relation can be expressed as

$$\bar{E} = \frac{K}{(t + t_0)^2} \tag{1}$$

where $\bar{E}$ is the mean neutron energy in keV, K is the slowing-down constant in keV μs^2, t is the measured time in microseconds after the source pulse and t_0 is a constant also in units of μs. For example, for a monoenergetic neutron source of 14 MeV, K is equal to 166.4 keV μs^2 and $t_0 = 0.11$ μs [5], but the parameters K and t_0 are expected to vary somewhat with the source energy. Our spallation neutron source, of course, provides a broad spectrum of neutron energies and therefore the determination of K and t_0 is more complicated analytically. The parameter t_0 represents the time needed by the neutrons after emission from the neutron source to reach the energy–time relation as given in Eq. (1). In the case of our present facility, t_0 can be evaluated by simulation, but is difficult to measure experimentally. On the other hand, the constant K can be determined precisely by simulation and measurements.

MCNPX simulations, for the energy–time relation, show that in the case of the present LSDS, taking into account the lead impurities and the influence of the Blue Room, the values of K and t_0 are 161 ± 5 keV μs^2 and 0.4 ± 0.1 μs, respectively.

Experimentally, the value of K was measured by neutron capture on different samples. Gamma emissions from the neutron capture were detected with a small (25 mm diameter and 5 mm thick) cylindrical cerium fluoride scintillator. The advantage of the CeF_3 scintillator is its small neutron capture cross-section and its fast scintillation decay-time constants (5 and 30 ns). After verifying that the results are insensitive to the position in the LSDS, the scintillator was positioned always at the same place ($X = 40$, $Y = -30$, $Z = 2$ cm) and covered with foils of different samples. Each

Table 1
Sample used for (n, γ) reactions, resonance energies and extracted parameters. Samples were not isotopically enriched

Isotope	Resonance (eV)	Used for	Isotope	Resonance (eV)	Used for
^{115}In	1.5	K, $\Delta E/\bar{E}$	^{197}Au	59	K
^{181}Ta	4.3	K, $\Delta E/\bar{E}$	^{59}Co	132	t_0, $\Delta E/\bar{E}$
^{197}Au	4.9	K, $\Delta E/\bar{E}$	^{65}Cu	230	t_0, $\Delta E/\bar{E}$
^{109}Ag	5.2	K, $\Delta E/\bar{E}$	^{55}Mn	336	t_0, $\Delta E/\bar{E}$
^{181}Ta	10.4	K, $\Delta E/\bar{E}$	^{63}Cu	579	t_0, $\Delta E/\bar{E}$
^{107}Ag	16.3	K, $\Delta E/\bar{E}$	^{56}Fe	1150	t_0, $\Delta E/\bar{E}$
^{111}Cd	27.5	K, $\Delta E/\bar{E}$			

sample has large neutron capture cross-sections at characteristic neutron resonance energies, as shown in Table 1.

As the time corresponding to the resonance energy is large compared to t_0 (for instance the 4.9-eV resonance of Au is at about 181 μs, according to the simulated values of K and t_0), the energy–time relation can be simplified to $E \simeq K/t^2$ for isotopes with neutron capture resonances less than 100 eV. This allows the value for K to be extracted from the data on resonance energy versus time. Then, with this value of K, t_0 is extracted from the measurements at higher capture resonance energies (>100 eV) using Eq. (1). Results are presented in Fig. 5 for each measured resonance energy and isotope. Values for K (161 ± 1 keV μs^2) and t_0 (0.37 ± 0.15 μs) are obtained from a horizontal fit, shown in the two plots.

As shown in the figure, the measured values of K and t_0 are in good agreement with the values obtained from the MCNPX simulations. A spread of up to 15% for the K values can be found in the literature: 183 [5], 179 [7], 155 [8], 180 [9] and 166 [10] keV μs^2. The differences are sometimes explained in terms of lead volume [13], different neutron production process with different particles types and incident energies, or different amounts of impurities in the lead.

3.2. Energy dispersion

The energy dispersion around the mean neutron energy is an important characteristics of the spectrometer. It has been shown in many references (for instance in Refs. [13,25]) that the theoretical energy resolution $\Delta E/\bar{E}$ is a function of the mean neutron energy $\bar{E}$

$$\Delta E/\bar{E} = 0.29 \cdot \sqrt{1 + \frac{1.96}{\bar{E}}} \quad \text{for } 0.1\,\text{eV} < \bar{E} < 200\,\text{eV} \tag{2}$$

where ΔE is the full width at half-maximum (FWHM) and $\bar{E}$ is the mean energy at a given time, in eV. At low energy (less than 10 eV), $\Delta E/\bar{E}$ is controlled by the thermal motion of the lead nuclei. At higher energy, the energy dispersion increases because of strong variations in the elastic and capture cross-sections of natural lead. In the ideal case, $\Delta E/\bar{E}$ can be as small as 29%. In practice, impurities in the lead increase the energy dispersion. Hydrogen, with its small mass, can have a marked effect even at very low concentrations and, of course, it cannot be completely eliminated from the air or from detectors and cables.

The energy resolution was evaluated by (n,γ) measurements on well-defined resonances with the CeF_3 scintillator. The measured resonance is a convolution of its intrinsic width and the resolution of the LSDS. These isotopes were the same as those used to determine K and t_0. Results are shown in Fig. 6 together with MCNPX simulations. Two calculations are presented, with and without impurities, the most important one being silver. As seen in the figure, the measurements and simulations agree well over a wide energy range. The measured resolutions at different energies show a minimum from $\simeq 10$ to 100 eV as expected and $\Delta E/\bar{E}$ increasing above 1 keV.

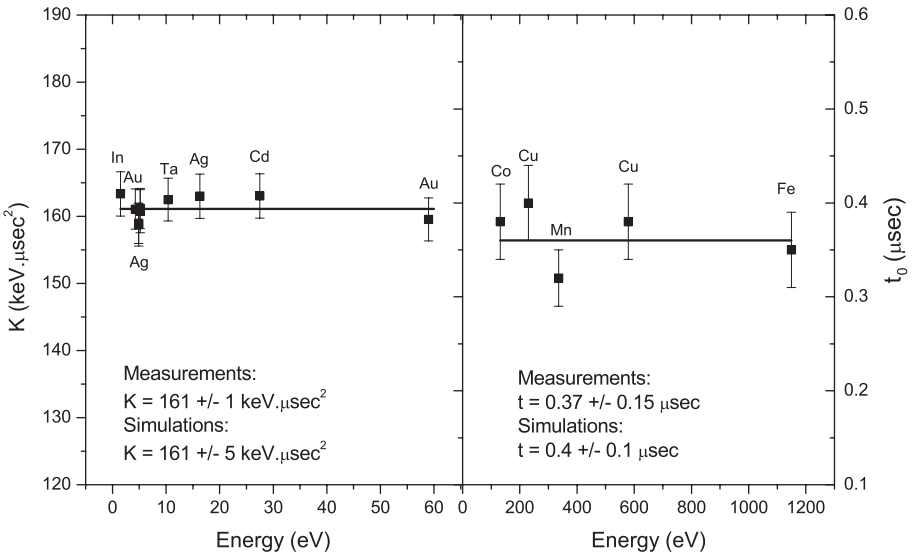

Fig. 5. Measurements of K and t_0 by (n,γ) reactions on different isotopes. The measured values are compared with simulations. The lines represent horizontal fits, giving values of K and t_0.

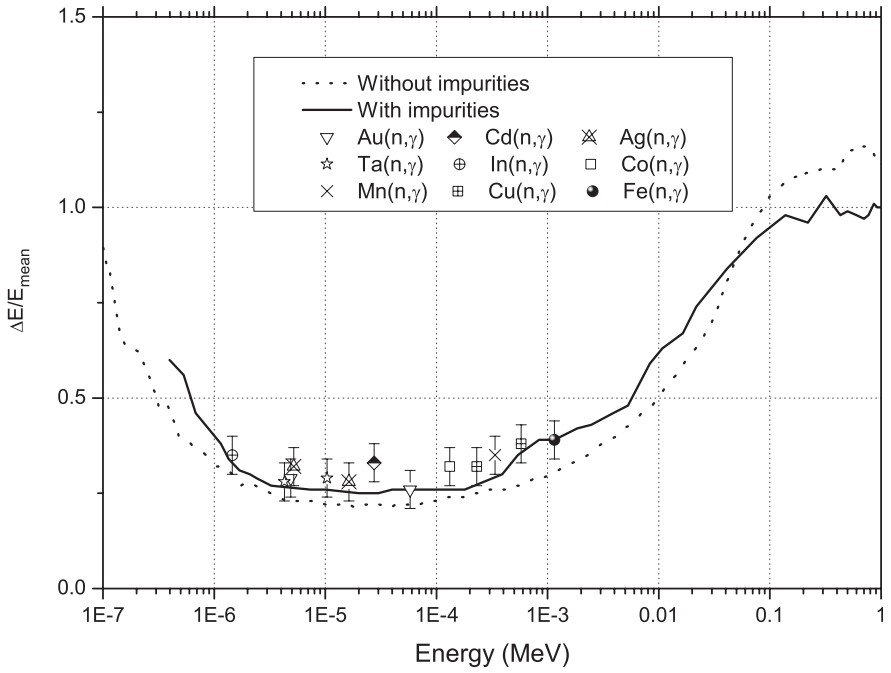

Fig. 6. Comparison of the measured $\Delta E/\bar{E}$ by (n,γ) reactions and MCNPX simulations.

The influences of the impurities result in a small but significant increase of the energy resolution for nearly all of the energy range. The simulation with impurities is in fact closer to the measurements, which reflects the importance played by the impurities even at the low concentrations found

in the present spectrometer. The calculated improvement in resolution with impurities for neutron energies above 50 keV is not understood at this time and warrants further investigation.

3.3. Neutron flux

The neutron flux is an essential parameter of the spectrometer, which must be measured to determine a cross-section. It can be simulated with MCNPX at different positions in the lead volume. The results in $n/cm^{-2}/MeV/proton$ can be compared with measurements. Two sorts of measurements were performed to evaluate the absolute neutron flux and its shape: (1) nuclear activation of selected materials and (2) time dependence of the fission of ^{235}U in a fission ion chamber.

The absolute neutron flux was measured at precise energies using a triple-foil activation technique [40]. This method consists of the activation of three foils of the same element in the LSDS. The foils are stacked together and their thickness is chosen so that the outer foils are opaque to neutrons at the resonance energy. To extract a value of the neutron flux, the difference between the average activity of the outer foils and the activity of the inner foil is measured. To obtain good results, the capture cross-section at the resonance should be at least a factor of 1000 larger than everywhere else. Three materials were chosen following this criteria, ^{115}In ($\sigma_{(n,\gamma)} = 2.92 \times 10^4$ barns at 1.46 eV), ^{197}Au ($\sigma_{(n,\gamma)} = 2.74 \times 10^4$ barns at 4.91 eV) and ^{186}W ($\sigma_{(n,\gamma)} = 1.54 \times 10^4$ barns at 18.81 eV). With this method, the neutron flux was measured at four different positions in the spectrometer. The average proton beam current for the activation was 70 nA and the irradiation time was 1 h. The results are presented in Fig. 7 for the four positions, three downstream and one upstream, compared to MCNPX simulations.

The simulations take into account the lead impurities and the Blue Room environment around the LSDS. As expected, the neutron flux decreases when distance from the target increases. The results from the triple-foil activations are in good agreement with the MCNPX simulations. This confirms the validity of the simulated neutron flux at three precise energies, but it does not give information on the neutron flux at other energies.

A second type of flux measurements was made with a ^{235}U fission chamber from the CEA Bruyères-le-Châtel, France. It contains a large amount of ^{235}U (803 μg ± 2%), known with precision and is usually used for absolute neutron flux measurements in a reactor environment. The active part of the chamber is a cylinder, 3 cm long and 0.5 cm in diameter. Because of the large amount of ^{235}U, only a low proton beam current is needed to obtain good counting statistics; this low current also avoids saturation of the detector and its electronics. Typically, the measurements were carried out at 20 Hz, with an average proton beam intensity of 8 nA. To extract the neutron flux from these measurements, the fission cross-section of ^{235}U, broadened with the LSDS energy resolution was used. With the energy resolution presented in Fig. 6 and the ^{235}U fission cross-section from ENDF/B-VI [41], the broadened fission cross-section of ^{235}U is calculated and presented in Fig. 8. The neutron flux was measured at six symmetric distances from the tungsten target, upstream and downstream: $(-50, 0, -10)$, $(-30, 0, -10)$, $(-10, 0, -10)$, $(10, 0, -10)$, $(30, 0, -10)$ and (50,0,10), with (X, Y, Z) as defined in Fig. 2(left), with the origin of the coordinates at the center of the tungsten target. Sample results for two of the positions are presented in Fig. 9, together with MCNPX simulations at these positions.

The shape and absolute values of the measured neutron flux are in good agreement with the MCNPX simulations. The uncertainty on the proton intensity measured with a current toroid is better than 5% and is not included in the error bars shown in the figure. At low neutron energies, less than 0.1 eV, the energy–time relation is not valid because thermal neutrons are randomly distributed throughout the time-of-flight spectrum. This explains the difference between simulation and measurement for $E_n < 0.1$ eV.

4. Fission measurements on small samples

One of the main goals of the LSDS at LANSCE is to measure the fission cross-section on a small

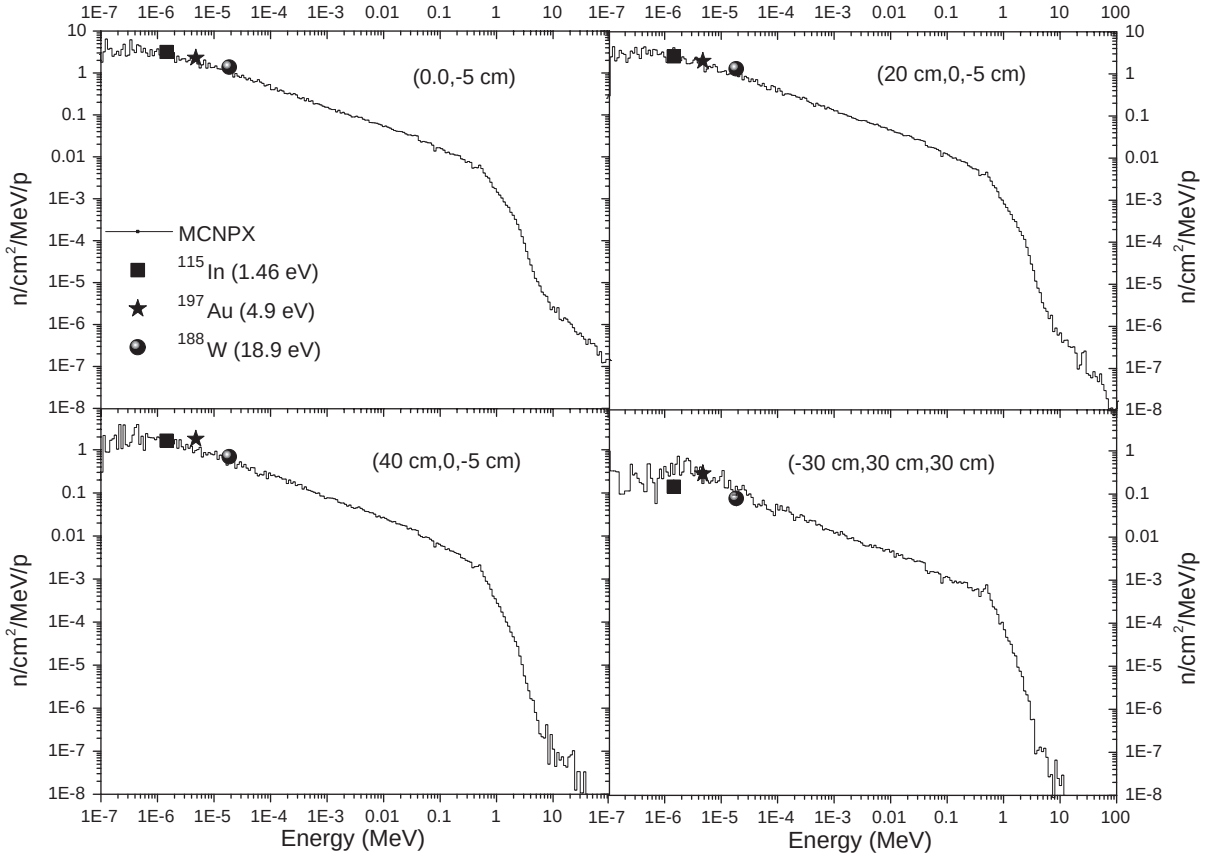

Fig. 7. Flux measurements by activation compared with MCNPX simulations at different positions referred with (X, Y, Z) coordinates as in Fig. 2.

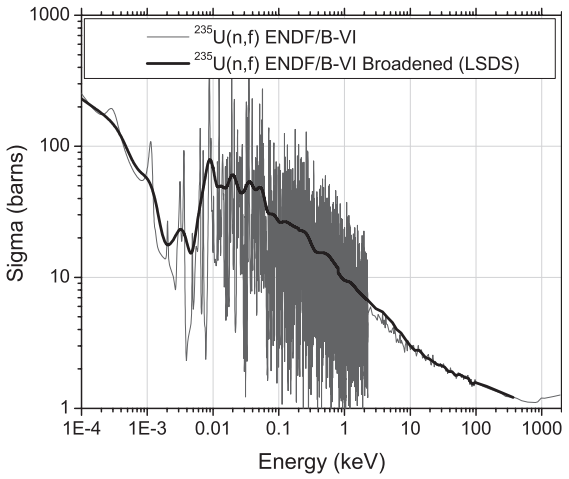

Fig. 8. Broadening of the fission cross-section of ^{235}U with the LSDS energy resolution, as given in Fig. 6. The original fission cross-sections for ^{235}U are taken from the ENDF/B-VI library.

quantity of the ^{235m}U isomer (10 ng), with an average proton beam intensity of 1 μA. First, however, we used larger samples of long-lived actinides to characterize the LSDS performance and to develop the measurement techniques. Two types of fission counters were used: gas ionization fission chambers and solid state fission chambers based on photovoltaic cells (solar cells). Both detectors were designed with gamma compensation in order to minimize the saturation induced by the spallation gamma rays and charged particles. The compensated fission chamber (CFC) consists of two parallel plate ionization chambers with the fissionable sample in one of the chambers. The chambers are arranged so that the difference in signals is recorded. Gamma rays or protons produced from the spallation process travel through the two chambers almost equally

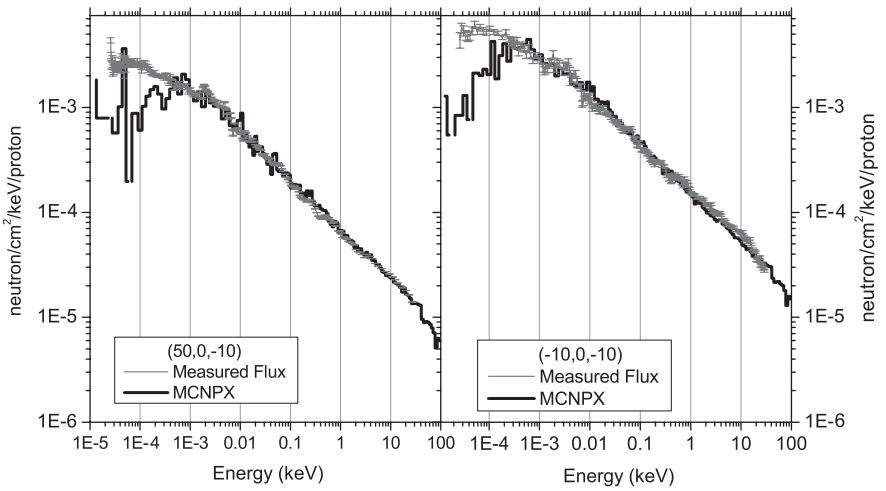

Fig. 9. Measured and simulated neutron fluxes for two different positions in the LSDS. The origin of the coordinates is taken at the center of the tungsten target.

and therefore cancel in the difference signal. Fission events, on the other hand, take place only in one chamber and therefore remain in the difference signal as desired events. The compensation with solar cells is the subject of Ref. [43] and will not be detailed here, but the principle is the same as for the CFC.

The following ^{235}U targets were fabricated and used in the measurements: 100 μg with a 10 nA time-averaged proton beam at 20 Hz, and 70, 10 and 1 μg of ^{235}U with 80 nA at 20 Hz. For quantities lower than 1 μg, the radioactivity signature from ^{235}U is too small to allow an accurate determination of the mass of the deposit by α or gamma counting (at 1 μg, the activity of ^{235}U is about 0.08 Bq). Therefore, to obtain a deposit with a known mass, an actinide with a shorter half-life, such as ^{239}Pu (at 1 μg, the activity of ^{239}Pu is about 2.3 kBq) is used. The samples were prepared by electro-deposition on Ti disks for the CFC or directly onto the surface of the solar cell.

In Fig. 10, measured fission cross-sections are presented for 70 μg of ^{235}U and 27 and 35 ng of ^{239}Pu. The CFC was used with the ^{235}U sample and the 35 ng ^{239}Pu sample, and the compensated solar cell was used with the 27 ng ^{239}Pu sample.

The measurement with ^{235}U was taken over 8 h at 40 nA and 20 Hz. For the ^{239}Pu, the measurements were accumulated over 3 h at 300 nA and 20 Hz. The neutron energy was calculated from the time-of-flight signal with $K = 161\,\text{keV}\,\mu\text{s}^2$ and $t_0 = 0.4\,\mu\text{s}$. For the ^{235}U data, the agreement between the broadened ENDF/B-VI data and the measurement is good, except between 2 and 4 eV probably due to tails in the neutron flux spectrum beyond the Gaussian function we used to broaden the ENDF/B-VI data. Interactions of neutrons with the detector materials could be a source of these tails. The signal was measured up to 1.5 ms after the proton pulse, which corresponds to 0.07 eV, with a digitizing rate of 20 MS/s. The good agreement between experiment and calculation is, to some degree, the result of a circular argument in that the calculated, MCNPX flux spectrum was validated by the (broadened) ^{235}U cross-section as indicated in Figs. 8 and 9.

For the ^{239}Pu measurements, the derivation of the cross-section is not based on a circular argument, and the agreement between the experimental results and the simulation is very good. Even with the counting statistics obtained in three hours of measurements, structures at 10 and 70 eV are clearly present. The beginning of the resonance at 0.3 eV is not clearly seen because of poor statistics and poor energy resolution. No background subtraction was possible because of the

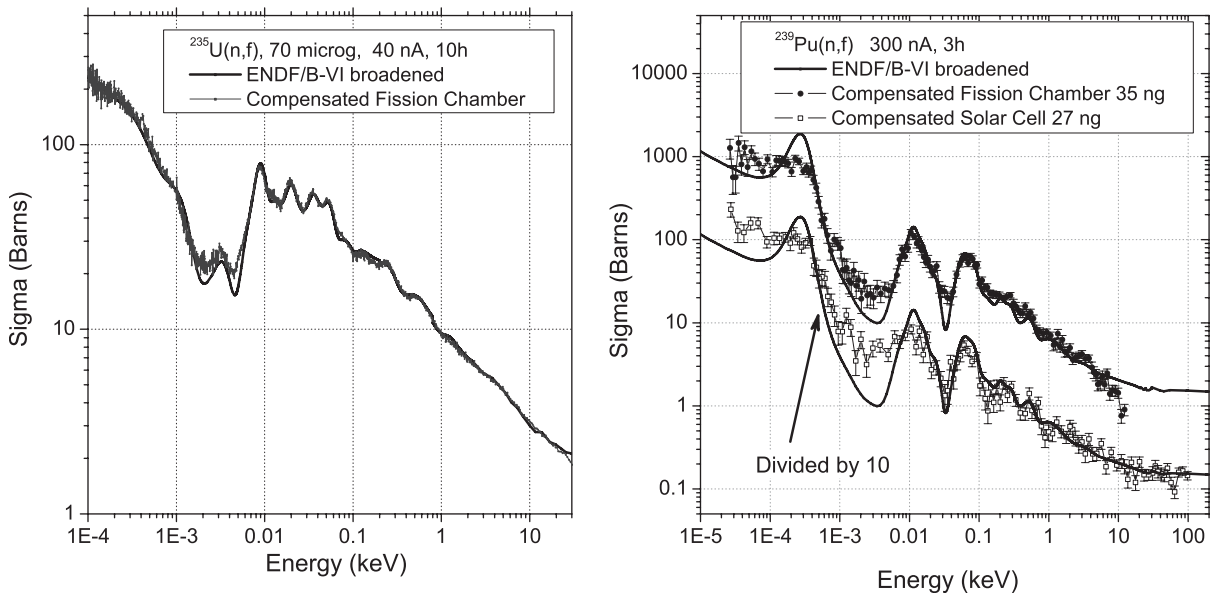

Fig. 10. Fission cross-section for ^{235}U (left) and ^{239}Pu (right). The data for the compensated solar cell are divided by 10 to avoid overlap. The measurements are normalized by hand to the broadened cross-sections such as presented for ^{235}U in Fig. 8.

limited beam time. The signal was measured up to 2.5 ms, which corresponds to thermal energy (0.026 eV) with a resolution of 50 ns.

For the compensated fission chamber, poor signal compensation of the gamma flash limited our measurements to times greater than 3.5 μs, which corresponds to neutron energies less than 10 keV. For the compensated solar cell, results were obtained up 100 keV because this detector and its associated preamplifier recovered more quickly after the gamma flash. In the future, a different pre-amplifier and an improved design for the CFC will be used to obtain better performance.

5. ^{235m}U target preparation

For the ^{235m}U(n, f) measurement with the LSDS, the preparation of the ^{235m}U ($t_{1/2} =$ 26 min) target is a challenge. One needs targets containing on the order of 10 ng total mass and having a ^{235m}U/^{235g}U (m/g) ratio that is as large as possible. Given the short half-life of the isomer, multiple targets will need to be prepared. Moreover, due to the changing m/g ratio caused by the decay of the isomer, each target will need to be measured in a time-sequenced fashion. This will enable a relative determination of σ_m/σ_g over the entire LSDS neutron energy range. It should be noted that this approach is "self-normalizing" in that the isomer decays entirely to the ground state. Thus exact knowledge of the total amount of uranium, isomer plus ground state, is not required.

The isomer, ^{235m}U, is populated in the alpha decay of ^{239}Pu with a total feeding of $>99\%$ [27]. Although the continuous collection of alpha recoils is an attractive approach toward obtaining the isomer with good purity, preliminary work [30,32] has not achieved good collection efficiencies for parent sources as large as are needed in the present experiment. Consequently, we are planning to scale-up a batchwise chemical extraction of ^{235m}U from a ^{239}Pu/HBr solution using a proven anion-exchange chemistry approach [30]. The previous work used ^{239}Pu sample sizes of 250 mg; for this work we envision using ~20 g quantities. This sample size may require that the chemistry be done in a glove box in a special building separate from LANSCE. In order to achieve the high uranium/plutonium separation

Table 2
Expected quantities of ^{235m}U and m/g ratio for different in-growth and chemistry-plus-transportation times, assuming a 20 g ^{239}Pu parent source and an 80% efficiency for the chemical separation and target preparation. The different symbols are used in Fig. 11

Chemistry target preparation and transport time (min)	15 min in-growth		25 min in-growth	
	^{235m}U (ng)	m/g	^{235m}U (ng)	m/g
30	4.8	0.59$^{\otimes}$	7.0	0.49*
40	3.6	0.40°	5.4	0.34$^{\diamond}$
50	2.8	0.28$^{\triangleright}$	4.1	0.24$^{\blacksquare}$

factor of $\simeq 10^{12}$ required for this measurement, multiple column chemistry steps are required. We will automate the chemistry and employ micro-chemistry in the final step to rapidly ($\simeq$ 20–30 min) produce pure samples of ^{235m}U, which will then be transported ($\sim$10 min) and installed in the LSDS for measurement. Table 2 contains growth and decay estimates for the quantity of ^{235m}U and m/g ratios that can be expected for different uranium in-growth and chemistry-plus-transportation times. We estimate that a minimum of ten ^{235m}U samples will be needed to achieve the desired cross-section accuracy (see the next section).

6. Simulations of the ^{235m}U fission cross-section measurement

In order to optimize the extraction of the σ_m cross-section, various target compositions are possible as outlined above. Two parameters, the total mass of final sample (^{235g}U + ^{235m}U) and its isomer-to-ground state (m/g) ratio, can play a key role in the accuracy of the measurements. To understand the influence of these two parameters and to optimize their values before the experiments are undertaken, simulations with MCNPX were carried out. The hypotheses are the following:

(1) at $t = 0$, when the target is installed in the LSDS, there are initially N_m^0 atoms of isomer and N_g^0 atoms of ground state; three masses of the total quantity of ^{235}U are considered: 5, 10 and 20 ng; and several m/g ratios are considered at $t = 0$.

(2) measurements of 2 h are repeated 10 times using a new target each time. During a 2-h measurement, a new histogram of the TOF signal is started each minute. This allows the count rate to be followed as a function of time after a new target has been installed in the LSDS. For each minute after $t = 0$ a new histogram is then obtained (a total of 120 histograms for a 2-h measurement). All ten measurements are then summed together;

(3) the decay of ^{235m}U during the course of the measurement is taken into account with a half-life of 26 min;

(4) the proton beam intensity is assumed to be 1 μA (time averaged);

(5) the ratio of cross-sections, σ_m/σ_g, is considered constant as a function of neutron energy and equal to 0.7. This is approximately the ratio predicted by Refs. [33,34] for neutron energies up to several hundred keV;

The count rate as a function of time, and for a given neutron energy, can be evaluated with the following equation:

$$C(t)^{E_n} = N_m^0 \cdot \phi^{E_n} \cdot \sigma_m^{E_n} \cdot e^{-\lambda \cdot t} + N_g^0 \cdot \phi^{E_n} \cdot \sigma_g^{E_n} + N_m^0 \cdot (1 - e^{-\lambda \cdot t}) \cdot \phi^{E_n} \cdot \sigma_g^{E_n} \quad (3)$$

where $C(t)^{E_n}$ is the count rate as a function of time t for the neutron energy E_n, ϕ^{E_n} is the neutron flux at the neutron energy E_n, $\sigma_m^{E_n}$ and $\sigma_g^{E_n}$ are the isomer and ground state fission cross-sections at the neutron energy E_n, respectively, and λ is equal to $\ln(2)/T_{1/2}$. Eq. (3) is then equivalent to

$$\frac{C(t)^{E_n}}{\phi^{E_n} \cdot \sigma_g^{E_n}} = N_m^0 \cdot [1 + (a-1) \cdot e^{-\lambda \cdot t}] + N_g^0 \quad (4)$$

where $a = \sigma_m/\sigma_g$. The neutron flux ϕ and the ground state fission cross-section σ_g are known, whereas the cross-section ratio a, N_m^0 and N_g^0 have to be determined. The simulation gives the count rate $C(t)$ and it is then possible to extract a

simulated fission cross-section for the isomer, together with the statistical uncertainties on a by fitting the count rate with Eq. (4). The results for the calculated fission cross-section of the isomer σ_m are presented in Figs. 11 and 12. The uncertainties shown take into account the average of ten measurements, each with new samples. In Fig. 11, the resulting uncertainties on the σ_m for the energy range 1–2 keV as a function of the m/g ratio are presented. Three different quantities of total ^{235}U (isomer plus ground state) are taken into account: 5, 10 and 20 ng (solid, dashed and dotted lines). Results for the expected sample quantities and m/g compositions given in Table 2 are presented with symbols defined in the table.

As seen in Fig. 11, the statistical uncertainties obtained with a 10 ng uranium target (isomer plus ground state) with a m/g ratio of ~0.6 are in the 12–15% range. The results on a 5 ng target with a similar m/g ratio are almost a factor of two larger. On the other hand, if the m/g ratio is less than 0.3, then rather large samples are required to obtain accuracies of better than 15%. Similar measurement accuracies are predicted at higher (up to 100 keV) and lower (down to 10 eV) neutron energies assuming the same energy interval of $\Delta E/\bar{E} = 35\%$. Below 10 eV, the cross-section falls off except at the isolated resonances, and the uncertainties therefore increase significantly.

A more detailed look at the energy dependence of the expected uncertainties is given in Fig. 12, where results are presented for three total masses and two m/g ratios for each mass. The energy intervals between dots are from 25 to 35% in $\Delta E/\bar{E}$. The uncertainties are shown to be larger in the low-energy-range region, because of the drop off in the number of neutrons in the 25 to 35% energy bin. One should keep in mind that the actual fission cross-section of ^{235m}U can differ from the assumed $0.7{\cdot}\sigma_g$ especially in the energy range of the resolved resonances. The count rate can be higher or lower than expected and the

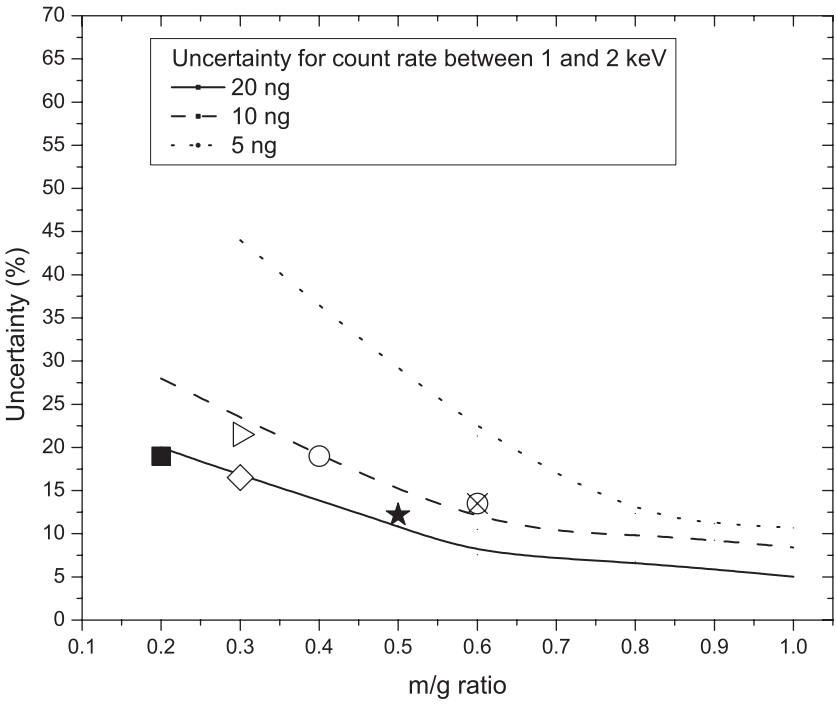

Fig. 11. Statistical uncertainty (1-sigma) on determining the cross-section of ^{235m}U for an incident neutron energy range of 1–2 keV for three different total masses (isomer plus ground state) as a function of m/g ratios (lines) compared to the six example target quantities and m/g compositions presented in Table 2 (see symbols definition in Table 2). These uncertainties are based on the average of ten measurements.

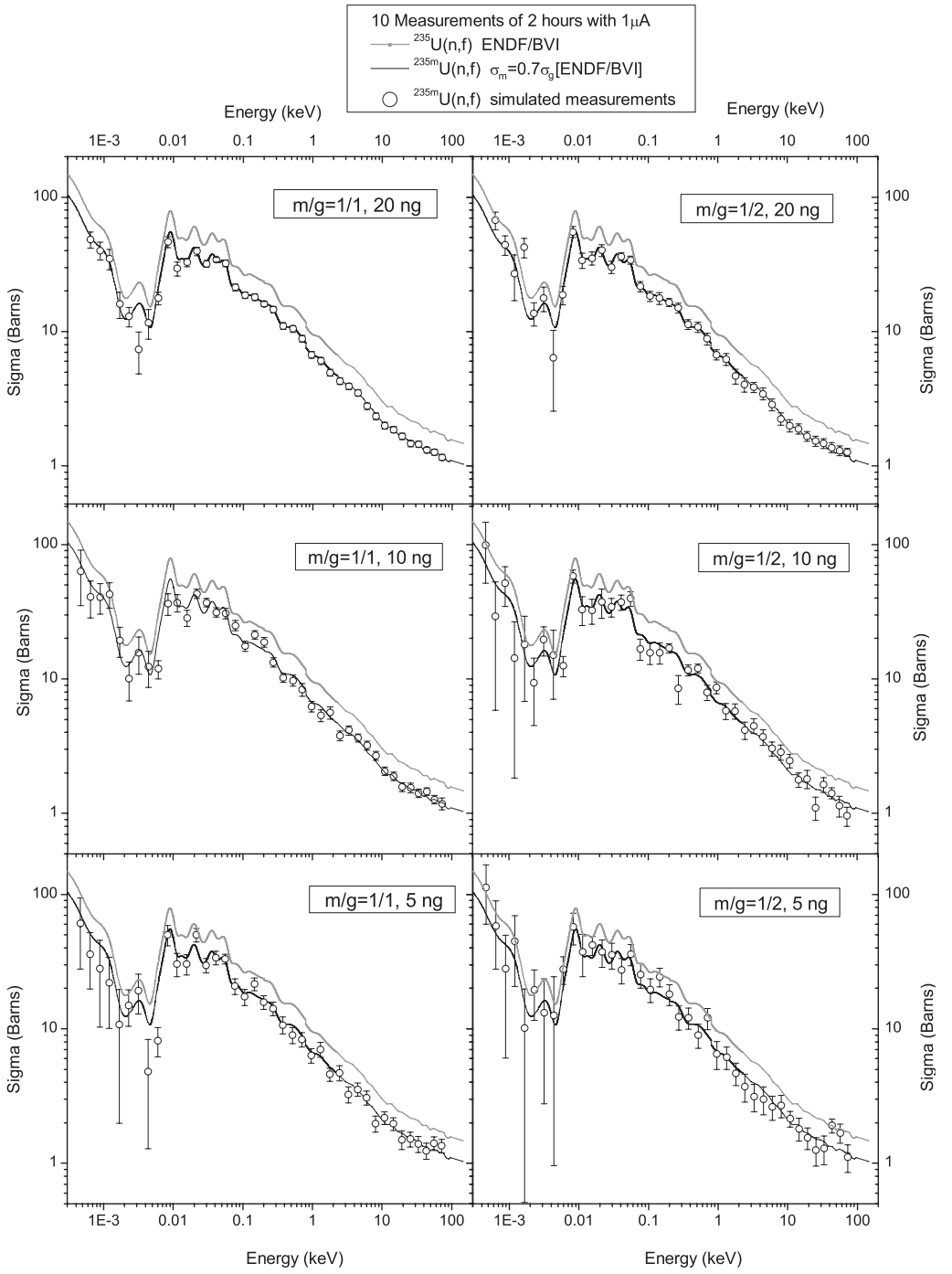

Fig. 12. Comparison of simulation of the ^{235m}U fission cross-section for different samples masses (isomer plus ground state) and different isomer-to-ground state ratios at the beginning of the measurement. In each of the six cases, the upper curve represents the fission cross-section for ^{235}U from ENDF/B-VI broadened by the experimental resolution of the LSDS and the lower is the same fission cross-section multiplied by 0.7, which represents the estimated cross-section for the isomer. The uncertainties on the simulated points are 1-sigma.

extracted uncertainties will change accordingly. But if the measured fission cross-section for the isomer is close to $0.7 \cdot \sigma_g$ or higher, the expected count rate will be enough to extract σ_m for neutron energies higher than 10 eV.

These simulations lead to the conclusion that the measurement of the fission cross-section of ^{235m}U with the LSDS will be possible under the following conditions:

- the total mass of a target is greater than 5 ng,
- the m/g ratio is at least 0.3 at the beginning of the measurement,
- each sample is measured for at least 2 h,
- ten measurements, each with fresh samples, are averaged,
- the average proton beam intensity is equal to 1 μA and
- the σ_m/σ_g ratio is in the vicinity of 0.7 or larger.

As shown in Section 5, these required conditions are compatible with the target preparation chemistry being developed in our laboratory.

7. Conclusion and perspective

The characteristics of the lead slowing-down spectrometer (LSDS) driven by the pulsed proton beam at LANSCE were measured with different methods and simulated with MCNPX. Measurements and simulations are in good agreement. The slowing-down constants, K and t_0 of the energy–time relation for the neutrons in the LSDS, were experimentally determined to be $161 \pm 1\,\text{keV}\,\mu\text{s}^2$ and $0.37 \pm 0.15\,\mu\text{s}$, respectively. The energy resolution was simulated and measured by (n,γ) reactions and indicate a minimum around 30% in $\Delta E/\bar{E}$. Gamma-flash issues were reduced by using compensated fission detectors and also by keeping the distance between the detector and the spallation target sufficiently large. A high neutron flux was obtained by spallation process with a 300 nA proton beam intensity, which allowed measurements of fission cross-sections on sub-microgram samples, such as for ^{239}Pu(n,f) with a sample mass of less than 30 ng.

A particularly challenging measurement, for which the LSDS is required, is that of the fission cross-section of the 26-min isomeric state of ^{235}U. Simulations of the count rate for realizable samples show that this fission cross-section σ_m can be determined with uncertainties between 10 and 15% for neutron energies higher than 10 eV. The uncertainties will be significantly larger for energies less than 10 eV. Other measurements are also being considered to utilize this new capability.

Acknowledgements

This work has benefited from the use of the Los Alamos Neutron Science Center at the Los Alamos National Laboratory. This facility is funded by the US Department of Energy and operated by the University of California under Contract W-7405-ENG-36. We are especially grateful to M.A. Taylor and E.B. Etuk for design of the support for the LSDS, to G.A. Chaparro for repeated assembly and disassembly of the LSDS, and to L.J. Bitteker and the LANSCE operations staff for providing the high quality pulsed proton beam from the Proton Storage Ring.

References

[1] M.S. Moore, et al., Experimental assessment of the performance of a proposed lead slowing down at WNR/PSR, in: R.W. Hoff (Ed.), Proceedings of the International Conference On Capture Gamma-Ray Spectroscopy, Pacific Grove, CA, USA, 1990, American Institute of Physics, New York, 1991, p. 253.

[2] T. Granier, L. Pangault, T. Ethvignot, R.C. Haight, X. Ledoux, V. Méot, Y. Patin, P. Pras, M. Szmigiel, R.S. Rundberg, J.B. Wilhelmy, Nucl. Instr. and Meth. Phys. Res. A 506 (2003) 149.

[3] R.C. Block, R.E. Slovacek, Y. Nakagome, R.W. Hoff, Technique for Fission Measurements of Highly Active and Weak Cross Section Actinides, in: J.W. Behrens, A.D. Carlson (Eds.), 50 Years with Nuclear Fission, Proceedings of an International Conference, Gaithersburg, Maryland, U.S., April 25–28, 1989, American Nuclear Society, Inc. La Grange Park, Illinois, 1989, p. 354.

[4] R.E. Slovacek, D.S. Cramer, E.B. Bean, J.R. Valentine, R.W. Hockenbury, R.C. Block, Nucl. Sci. Eng. 62 (1977) 455.

[5] A.A. Bergman, A.I. Isakov, I.D. Murii, F.L. Shapiro, I.V. Shtranikh, M.V. Kazarnovsky, Proceedings of the

First International Conference on Peaceful Uses of Atomic Energy, Geneva, vol. 4, 1955, p. 135.
[6] MCNPX version 2.5d, Los Alamos National Laboratory Reports LAUR 03-5916 and LAUR 02-2607, http://mcnpx.lanl.gov
[7] F. Mitzel, H.S. Plendl, Nukleonik 6 (1964) 371.
[8] H. Wakabayashi, A. Sekiguchi, M. Nakazawa, O. Nishino, J. Nucl. Sci. Technol. 7 (1970) 487.
[9] J.C. Chou, H. Werle, J. Nucl. Energy 27 (1973) 811.
[10] M. Sawan, R. Conn, Nucl. Sci. Eng. 54 (1974) 127.
[11] A. Yamanaka, I. Kimura, S. Kanazawa, K. Kobayashi, S. Yamamoto, Y. Nakagone, Y. Fujita, T. Tamai, Nucl. Sci. Technol. 30 (1993) 863.
[12] R. Pourimani, U. Olejniczak, Yu.P. Popov, M. Przytula, R. Wojtkiewicz, Nucl. Inst. and Meth. Phys. Res. A 488 (2002) 226.
[13] A. Abánades, et al., Nucl. Inst. and Meth. Phys. Res. A 478 (2002) 577.
[14] A.A. Alexeev, A.A. Bergman, A.N. Volkov, O.N. Goncharenko, A.P. Zhukov, A.D. Perekrestenko, N.M. Sobolevsky, New 100-ton lead slowing-down spectrometer of the IRN RAS (S-100)—Characteristics, tasks, results, Proceedings of XVI International Workshop on Physics of Nuclear Fission, IPPE, Obninsk, Russia, October 7–10, 2003.
[15] H.T. Maguire, C.R.S. Stopa, R.C. Block, D.R. Harris, R.E. Slovacek, J.W.T. Dabbs, R.J. Dougan, R.W. Hoff, R.W. Lougheed, Nucl. Sci. Eng. 89 (1985) 293.
[16] H.T. Maguire, D.R. Harris, R.C. Block, R.E. Slovacek, J.W.T. Dabbs, R.J. Dougan, R.W. Hoff, R.W. Lougheed, Nucl. Sci. Eng. 89 (1985) 293.
[17] B. Alam, R.C. Block, R.E. Slovacek, R.W. Hoff, Nucl. Sci. Eng. 99 (1988) 267.
[18] Y. Danon, R.E. Slovacek, R.C. Block, R.W. Lougheed, R.W. Hoff, M.S. Moore, Nucl. Sci. Eng. 109 (1991) 341.
[19] K. Kobayashi, S. Yamamoto, S. Lee, H.J. Cho, H. Yamana, H. Moriyama, Y. Fujita, Nucl. Sci. Eng. 139 (2001) 273.
[20] Y. Danon, M.S. Moore, P.E. Koehler, P.E. Littleton, G.G. Miller, M.A. Ott, L.J. Rowton, W.A. Taylor, J.B. Wilhelmy, M.A. Yates, A.D. Carlson, N.W. Hill, R. Harper, R. Hilko, Nucl. Sci. Eng. 124 (1996) 482.
[21] Y. Nakagome, R.C. Block, R.E. Slovacek, E.B. Bean, Phys. Rev. C 43 (1991) 1824.
[22] R.C. Block, Y. Nakagome, R.E. Slovacek, E.B. Bean, Trans. Am. Nucl. Soc. 28 (1978) 719.
[23] R.E. Slovacek, D.S. Cramer, E.B. Bean, J.R. Valentine, R.W. Hockenbury, R.C. Block, Nucl. Sci. Eng. 62 (1977) 455.
[24] R.C. Block, R.W. Hockenbury, R.E. Slovacek, E.B. Bean, D.S. Cramer, Phys. Rev. Lett. 31 (1973) 247.
[25] L. Perrot, Validation des bases de données de sections efficaces par l'utilisation d'un spectromètre à temps de ralentissement au plomb entre 0,1 eV et 30 keV. Méthodologie—Résultats, Ph. D. Thesis, Grenoble, France, 2001.
[26] K. Kobayashi, S. Lee, S. Yamamoto, H.J. Cho, Y. Fujita, J. Nucl. Sci. Technol. 39 (2002) 111.
[27] R.B. Firestone, et al., Table of Isotopes, in: C.M. Baglin (Ed.), Eighth ed., 1998 update, Wiley Interscience, New York.
[28] V.I. Zhudov, A.G. Zelenkov, V.M. Kulakov, M.I. Mostovoi, B.V. Odinov, Pis'ma Zh. Eksp. Toer. Fiz. 30 (1979) 549;
V.I. Zhudov, A.G. Zelenkov, V.M. Kulakov, M.I. Mostovoi, B.V. Odinov, JETP Lett. 30 (1979) 516.
[29] A. D'Eer, C. Wagemans, M. Nève de Mévergnies, F. Gönnenwein, P. Geltenborg, M.S. Moore, J. Pauwels, Phys. Rev. C 38 (1988) 1270.
[30] W.L. Talbert Jr., J.W. Starner, R.J. Estep, S.J. Balestrini, M. Attrep Jr., D.W. Efurd, F.R. Roensch, Phys. Rev. C 36 (1987) 1896.
[31] V.I. Mostovoi, G.I. Ustroiev, At. Energ. 57 (1984) 241.
[32] D.A. Shaughnessy, et al., Abstr. Am. Chem. Soc. http://www.cofc.edu/~nuclear/2003NewOrleans225Abstracts.pdf (2003) 53.
[33] J.E. Lynn, A.C. Hayes, Phys. Rev. C 67 (2003) 014607.
[34] W. Younes, H.C. Britt, Phys. Rev. C 67 (2003) 024610.
[35] X. Ledoux, J. Sigaud, J.P. Lochard, Y. Patin, P. Pras, C. Varignon, J.M. Laborie, Y. Boulin, Expérience CIRENE, Description et Résultats, Rapport CEA-R-6030, ISSN 0429-3460, 2003.
[36] P.W. Lisowski, C.D. Bowman, G.J. Russell, S.A. Wender, Nucl. Sci. Eng. 106 (1990) 208.
[37] K. Corzine, Ph.D. Thesis, Georgia Institute of Technology, Atlanta, USA, 2004.
[38] The Maximum Integrated Data Acquisition System (MIDAS), developed at TRIUMF and PSI, http://midas.triumf.ca/
[39] ROOT, an Object Oriented Data Analysis Framework, http://root.cern.ch/.
[40] CERN Yellow Report 99–11, The TARC experiment (PS211): neutron-driven nuclear Transmutation by Adiabatic Resonance Crossing, available online at http://doc.cern.ch/cernrep/1999/99-11/99-11.html.
[41] ENDF/B-VI file, Material 9228, Revision 5, http://www.nndc.bnl.gov.
[43] M. Petit, T. Ethvignot, T. Granier, R.C. Haight, J.M. O'Donnell, D. Rochman, S.A. Wender, E.M. Bond, T.A. Bredeweg, D.J. Vieira, J.B. Wilhelmy, Y. Danon, 2005 (submitted to Nucl. Inst. and Meth. A).